Available online at www.sciencedirect.com
SCIENCE DIRECT®

International Journal of Heat and Fluid Flow 24 (2003) 67–76

International Journal of
HEAT AND FLUID FLOW

www.elsevier.com/locate/ijhff

Unsteady laminar flow and convective heat transfer in a sharp 180° bend

Yongmann M. Chung [a], Paul G. Tucker [a,*], D.G. Roychowdhury [b]

[a] Fluid Dynamics Research Centre, Department of Engineering, University of Warwick, Coventry CV4 7AL, UK
[b] Core Engineering Section, Indira Gandhi Centre for Atomic Research Centre, Kalpakkam 603 102, India

Received 7 February 2002; accepted 4 August 2002

Abstract

Unsteady laminar flow and heat transfer in a sharp 180° bend is studied numerically to investigate a convective heat transfer regime of especial relevance to electronic systems. Due to the high geometrical aspect ratios occurring in the practical application, two-dimensional unsteady simulations are considered. The two-dimensionality assumption adopted is validated by three-dimensional test simulations. Unsteady heat transfer simulations are performed for $50 \leqslant Re \leqslant 1000$. Results show that the flow remains steady until $Re \approx 600$. In this steady regime, the re-attachment length increases gradually with the Reynolds number. For $Re > 600$, the flow becomes unsteady with large-scale vortices emanating from the sharp edge dominating the flow field. Flow oscillation causes a substantial reduction in the re-attachment length and a dramatic heat transfer enhancement. As the vortices move downstream, the Nusselt number along the wall oscillates significantly. The correlation between the flow structure and the heat transfer is found to be strong.

Keywords: Laminar; Unsteady; Heat transfer; Numerical simulation; Sharp 180° bend

1. Introduction

As the demand for compact, high performance electronic systems increases, their thermal control is becoming an everincreasing issue. Careful thermal management is essential for the design of such systems. Generally, electronic systems contain many circuit boards and internal geometries can have numerous corners and recesses. These geometrical features can cause abrupt changes in flow direction, separation and consequently large-scale vortices. An electronic central processor unit exhibiting some of these attributes is shown in Fig. 1(a). The subsequent convection of vortices gives rise to significant flow unsteadiness and consequently temporal heat transfer variations.

Despite its high industrial relevance, convective heat transfer due to unsteady separated flow around circuit boards (see region A in Fig. 1(b)) has received relatively little attention compared to unsteady cooling over integrated circuit arrays. Motivated by integrated circuit array cooling, Ghaddar et al. (1986) performed laminar periodic grooved channel flow simulations. They found that by using a subcritical oscillation heat transfer can be increased by up to 15%. Similarly, Kim et al. (1997) used an inflow oscillation to increase the hear transfer, finding a particular frequency for the maximum heat transfer enhancement. Unsteady flow, impinging jets have also been used to remove localised heat loads in electronics package (Beitelmal et al., 2000; Chung et al., 2001a; Chung et al., 2002).

In this study, the flow around a sharp 180° bend shown in Fig. 2 is considered as a simplification to the flow around circuit boards. Massive flow separation occurs as the flow passes around the bend and this at relatively low Reynolds numbers can cause an oscillatory downstream flow (Chung et al., 2001b). In the work of Ghaddar et al. (1986), Kim et al. (1997), and Chung et al. (2002) it is found that the flow oscillations can significantly affect laminar convective heat transfer. Therefore, understanding of the unsteady heat transfer in sharp 180° bends is important.

---

[*] Corresponding author. Tel.: +44-24-7655-28242; fax: +44-24-7655-23387.
E-mail address: pgt@eng.warwick.ac.uk (P.G. Tucker).

0142-727X/02/$ - see front matter © 2002 Elsevier Science Inc. All rights reserved.
PII: S0142-727X(02)00202-3

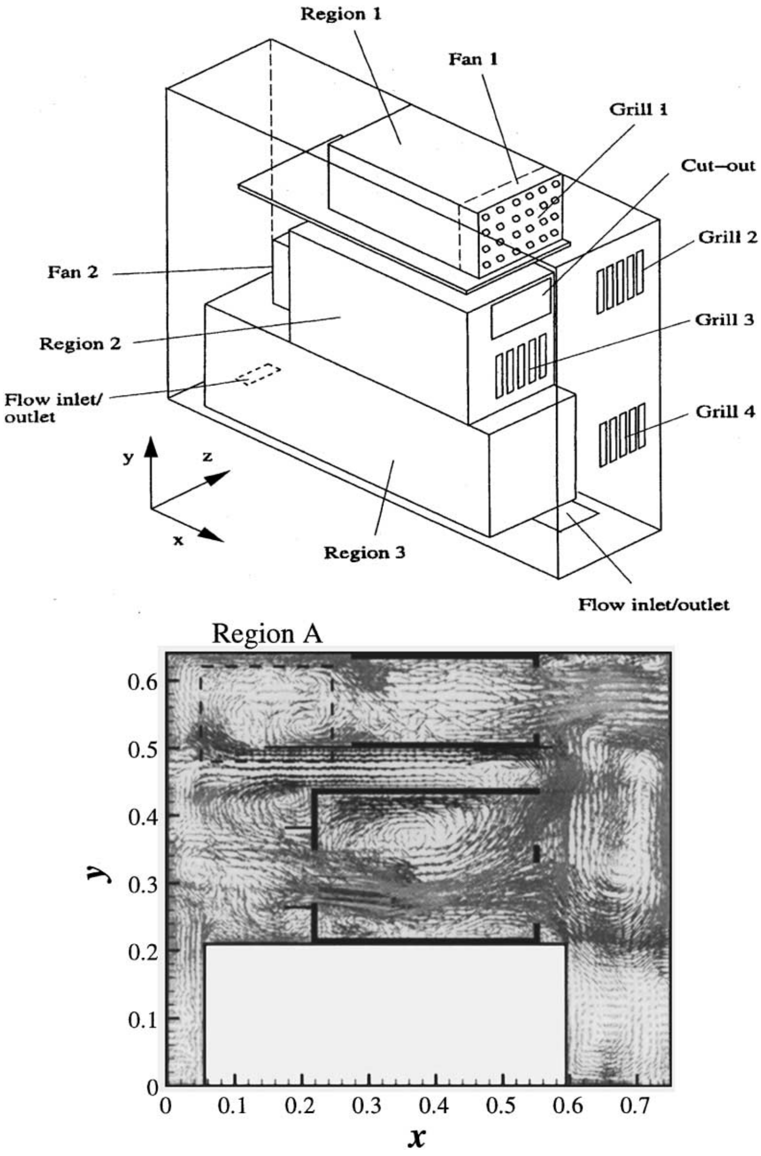

Fig. 1. Schematic diagram of an idealised electronics system flow (upper) and velocity vectors in x–y plane (lower).

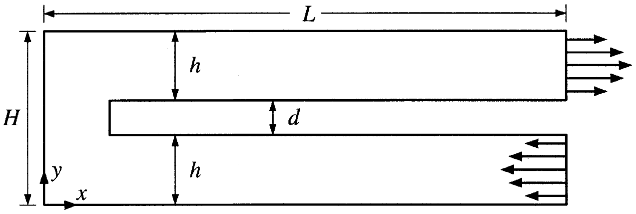

Fig. 2. Problem definition and computational domain.

Previous studies on the flow around sharp 180° bends have mostly focused on higher ($Re \geqslant 10^4$) Reynolds numbers (Metzger and Sahm, 1986; Chyu, 1991; Hirota et al., 1999; Mochizuki et al., 1999; Liou et al., 2000). At these Reynolds numbers, industrial applications include ventilation piping systems and inter-cooling passages in gas turbine blades. In contrast, for electronic systems the Reynolds number is much lower and typically in a range of $Re \leqslant 5000$.

In the present study, unsteady numerical simulations are performed for $Re \leqslant 1000$ flows in a 180° sharp bend. Due to the massive separation, the flow unsteadiness and heat transfer in these are much stronger than for U-bends. Unsteady flow characteristics and the related convective heat transfer are analysed.

2. Problem definition

As noted earlier, the flow configuration considered in this study is as shown in Fig. 2. Flow enters the computational domain at the right end of the lower channel and exits at the right end of the upper one. The lower and upper channels are referred to as inlet and outlet channels, respectively. The length, height and width of the computational domain are L, H and W, respectively. The channel height is h and the plate thickness d. The Reynolds number is defined as $Re = U_\mathrm{m}h/\nu$, where U_m is the bulk-mean velocity and ν kinematic viscosity.

In order to investigate the downstream flow recovery after the sharp bend, the computational domain is long, $L = 20h$. In this study, $d/h = 0.1$ is chosen as representative of a typical electronics system value. In these, the aspect ratios (W/h, W/d) are generally high and the flow in the central part can be regarded as two-dimensional. To validate this two-dimensionality assumption, three-dimensional test simulations are also performed (see later).

3. Numerical method

3.1. Governing equations

For an incompressible flow, the unsteady Navier–Stokes equations can be written in the following tensor form:

$$\frac{\partial u_i}{\partial x_i} = 0, \tag{1}$$

$$\frac{\partial u_i}{\partial t} + \frac{\partial}{\partial x_j}(u_i u_j) = -\frac{\partial p}{\partial x_i} + \nu \frac{\partial^2 u_i}{\partial x_j^2}, \tag{2}$$

$$\frac{\partial T}{\partial t} + \frac{\partial T u_i}{\partial x_i} = -\frac{k}{\rho C_p}\frac{\partial^2 T}{\partial x_i^2}, \tag{3}$$

where u_i is the instantaneous velocity in the x_i direction, p is the pressure, and T is the temperature. Here ρ is the fluid density, k thermal conductivity and C_p the specific heat capacity. The subscripts i, j, k take values of 1, 2, 3 to denote the streamwise (x), normal to the wall (y), and spanwise (z) directions, respectively.

3.2. Boundary conditions

At the inlet, a parabolic velocity profile is provided. At the outlet, to allow flow to pass without any distortion or reflections, the following convective boundary condition of Pauley et al. (1990) is applied:

$$\frac{\partial u_i}{\partial t} + U_\mathrm{c}\frac{\partial u_i}{\partial x} = 0, \tag{4}$$

where U_c is the convective velocity at the exit. In this study, U_c is equal to the bulk-mean velocity, U_m. At solid walls, the no-slip boundary conditions are used.

To approximate thermal conditions occurring in electronics, temperature boundary conditions are set. The temperature of the incoming flow is constant at T_i. The temperature of the lower wall, located at $y = h + d$, after bend is T_w. For relevance to heat transfer from circuit boards $T_\mathrm{w} > T_\mathrm{i}$ and the upper wall, located at $y = H$, is adiabatic. The temperature at the remaining walls is constant at T_i.

3.3. Numerical scheme

The governing equations are solved using standard finite volume methods (see Tucker and Pan, 2001; Roychowdhury et al., 1999). Time integrations involve using a second-order Crank–Nicholson scheme for both convective and viscous terms. For spatial discretisation, second-order central differences are used. The coupling between pressure and velocity is achieved by the SIMPLEC algorithm of Van Doormaal and Raithby (1984). Most simulations are run on a 569 × 143 non-uniform grid. A few low Reynolds number cases ($Re < 300$) where the flow is steady are run on a 285 × 71 grid. The effects of the temporal resolutions are investigated by successively halving time steps until no substantial differences are observed. Time steps of $\Delta t = 0.01$ are used.

4. Results and discussion

4.1. Validation

To the best of the authors' knowledge, there are no experimental data for two-dimensional laminar flows in a sharp 180° bend. Consequently, the present numerical results cannot be compared directly with measurements. Instead, the validation of the numerical predictions has been performed with carefully selected test cases.

The code used is intensively tested for Tollmien–Schlichting (T–S) wave propagation fidelity prior to moving on to high resolution two-dimensional simulations. As with Chung et al. (1997), the temporal and spatial accuracy of the present numerical method is verified by simulating the spatial development of an instability wave in a laminar channel flow. For theoretical investigations of travelling T–S wave instabilities, the plane Poiseuille flow can be regarded as a prototype case. This is because unlike the Blasius boundary layer flow, the base flow is strictly parallel and has an exact solution of the Navier–Stokes equations (Kleiser and Zang, 1991). A two-dimensional laminar channel flow between two parallel plates located at $y = 0$ and $y = 2$ is considered. The streamwise length of the computational domain is 50. This is equivalent to approximately 10 T–S wave lengths. The Reynolds number based on the centreline velocity and channel half-width h is $Re = 5000$.

At the inflow boundary, a T–S wave obtained from the eigensolution of the Orr–Sommerfeld equation is superimposed on a laminar parabolic profile. More details of the implementation of the inflow boundary condition can be found in Chung et al. (1997). Fig. 3 shows the disturbance streamfunction contours of T–S waves. Broken lines represent the negative values. The

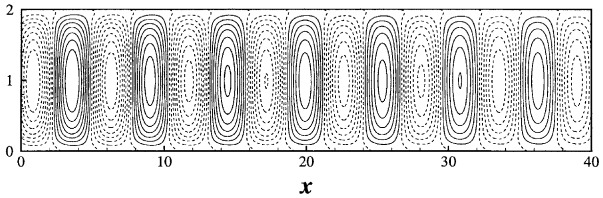

Fig. 3. Plot of x–y plane disturbance streamfunction.

typical counter-rotating T–S waves are clearly seen. As the flow goes downstream, the strength of the disturbances decreases and fewer contour lines appear. The disturbance kinetic energy decays exponentially $e^{-\alpha_I t}$. The predicted decay rate of the disturbance is within 2% of the analytic value of $\alpha_I = 0.0106$. The wave length is also in good agreement with the analytic value of $\alpha_R = 1.1557$.

Another widely used benchmark problem to examine the accuracy of numerical methods is the flow over a backward-facing step. This flow is an ideal test case for complex flow simulations because it involves flow separation, a free-shear layer, re-circulation, re-attachment, and redevelopment. The geometry is the same as in the experiments of Armaly et al. (1983). The expansion ratio of the step height (h) to the entrance channel height is 1:2 and the domain is $30h$. Fig. 4 shows the calculated re-attachment length as a function of Re. The experimental and numerical data of Armaly et al. (1983) and the predictions of Kim and Moin (1985) are also included. The present results compare well with the other data.

For further validation, three-dimensional, low-aspect ratio U-bend flow simulations are conducted (see Fig. 5). The flow configuration is chosen to match the experiment of Hille et al. (1985). The duct has a curvature ratio $R/D = 6.5$, where R is the radius of curvature and D the hydraulic diameter. The inner width a and height b of the duct are taken as 1.0 (i.e., an aspect ratio of unity). The lengths of the duct before and after the bend are taken as 10 times the hydraulic diameter. At inlet, a fully developed velocity profile is applied. The Reynolds number is defined as $Re = (U_m D/\nu)$. Simulations are performed for two Reynolds numbers, $Re = 203$ and 574. The corresponding Dean numbers ($K = Re(D/R)^{1/2}$) are $K = 80$ and 226, respectively.

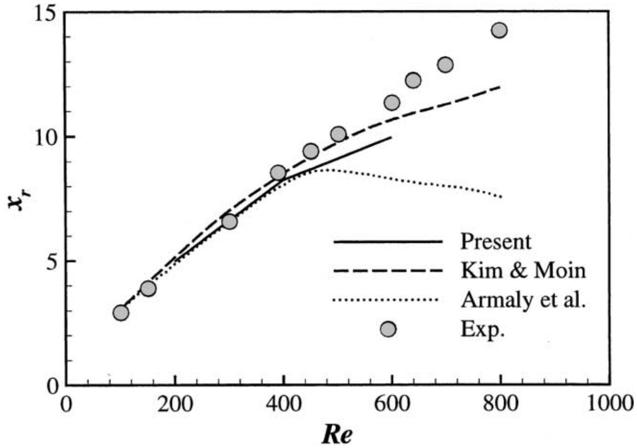

Fig. 4. Re-attachment length as a function of Re.

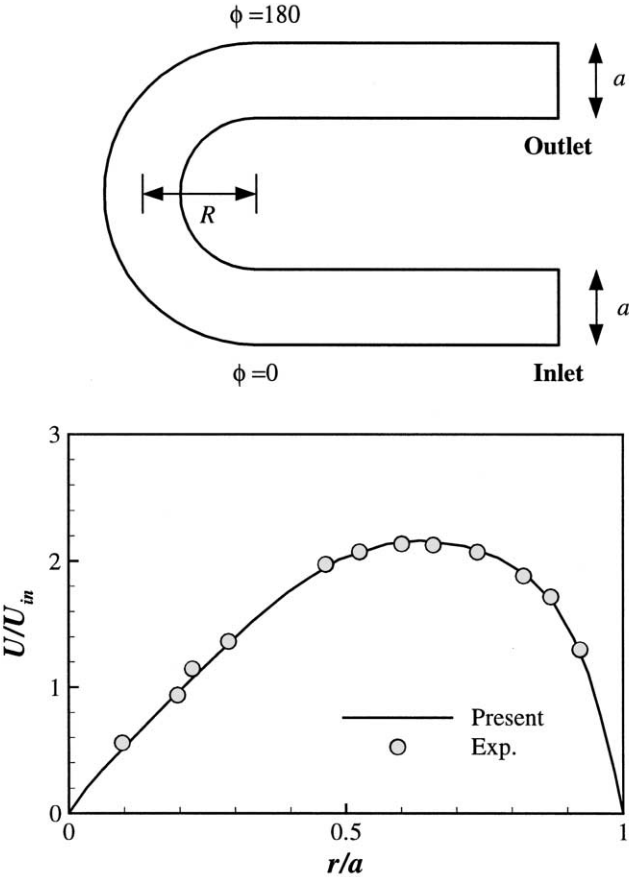

Fig. 5. Schematic diagram of U-bend flow (upper) and mainstream velocity as a function of radial location r at duct mid-height and $K = 226$ (lower).

The radial variations of azimuthal velocity compares well with measurements of Hille et al. (1985) at various locations along the mid-span of the duct. Fig. 5 shows the normalised azimuthal velocity at $\phi = 18°$. Acceleration of the flow along the outer wall is clearly captured in the simulation. Due to the smooth geometric change, correctly flow separation is not predicted. However, counter-rotating streamwise vortices and an additional pair of counter-rotating vortices near the outer wall are predicted (not shown here) and these are in good agreement with flow visualisation evidence. At $Re = 574$ ($K = 226$), an additional pair of counter-rotating vortices is found near the outer wall. These findings are totally consistent with those of Ghia and Sokhey (1977).

4.2. Two-dimensionality assumption

In low Reynolds number laminar flow simulations, the two-dimensionality assumption has been commonly chosen when the aspect ratio is high. For the completeness of the study, however, test simulations have been performed for three-dimensional 180° sharp bend flow to validate the two-dimensionality assumption used. Two effects have been considered separately: one is the side wall effect and the other is the three-dimensional instability effect. The side wall effects are found to be small even at a moderate aspect ratio (AR = 5) as the secondary vortices are confined to the side wall region. In the central part, therefore, the general flow structure can be regarded as two-dimensional. In typical electronics systems, the aspect ratio (W/h, W/d) is generally high. It is also worth noting that Brederode and Bradshaw (1978) recommends AR > 10 to avoid significant side wall effects for a backward-facing step flow.

In order to investigate the three-dimensional instability effect, a three-dimensional test simulation has been performed with periodic boundary conditions in the spanwise (z) direction. It begins with a flow field obtained from the corresponding two-dimensional simulation. At the beginning of the simulation, random perturbations are imposed on the initial flow field. The magnitude of the w velocity component fluctuations decreases in time and the flow field remains two-dimensional, indicating that the flow oscillations are mainly a two-dimensional phenomenon. The instantaneous C_f distributions at several spanwise locations are shown in Fig. 6. It is found that the spanwise variation of C_f remains small.

4.3. Flow characteristics

Numerical simulations are made for $50 \leqslant Re \leqslant 1000$. The flow is found steady until $Re \approx 600$. For $Re > 600$, it becomes oscillatory. This is clear from Fig. 7, showing the velocity time history at $x = 20$ and $y = 1.6$ for $Re = 500$, 700 and 1000. At $Re = 500$, velocity fluctuations decay after an initial transient period ($0 \leqslant t \leqslant 60$) and so the flow field is almost steady. As the Reynolds number increases, oscillations are sustained and the flow becomes unsteady. Significant quasi-periodic velocity variations can be seen at $Re = 700$ and 1000. The dominant low frequency component corresponds to the vortex shedding from the sharp corner (see also Fig. 13). In Fig. 8 several other frequencies are also seen, suggesting the complexity of the flow field.

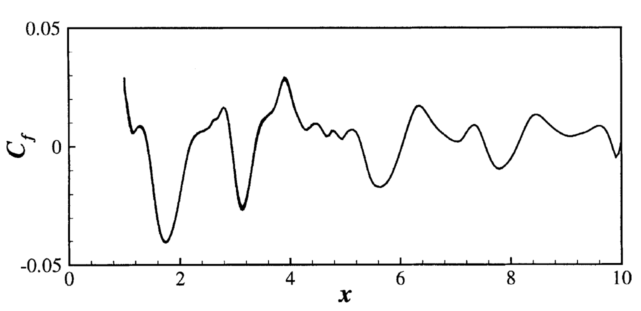

Fig. 6. Instantaneous skin friction coefficient (C_f) distributions at several spanwise locations.

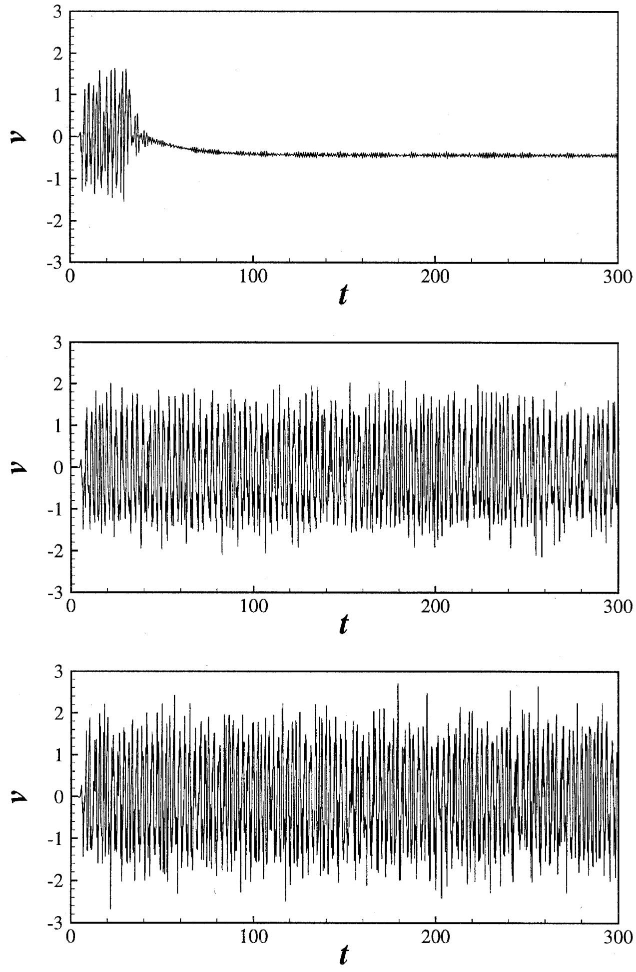

Fig. 7. Instantaneous v velocity at the measurement point ($x = 15$, $y = 1.6$): (a) $Re = 500$, (b) $Re = 700$ and (c) $Re = 1000$.

It is evident that flow unsteadiness significantly affects the mean flow field. Time-mean streamlines and velocity vectors are shown in Figs. 9 and 10, respectively, for the three Reynolds numbers. As the onset of

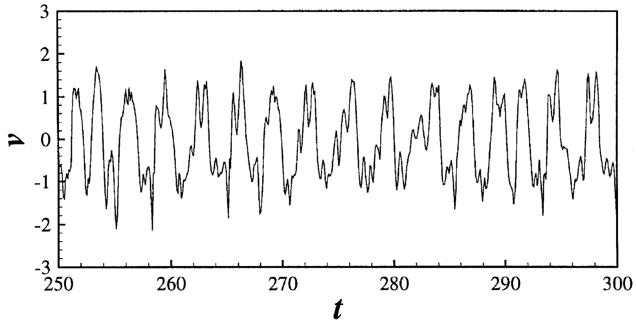

Fig. 8. Instantaneous v velocity at the measurement point ($x = 15$, $y = 1.6$) at $Re = 700$.

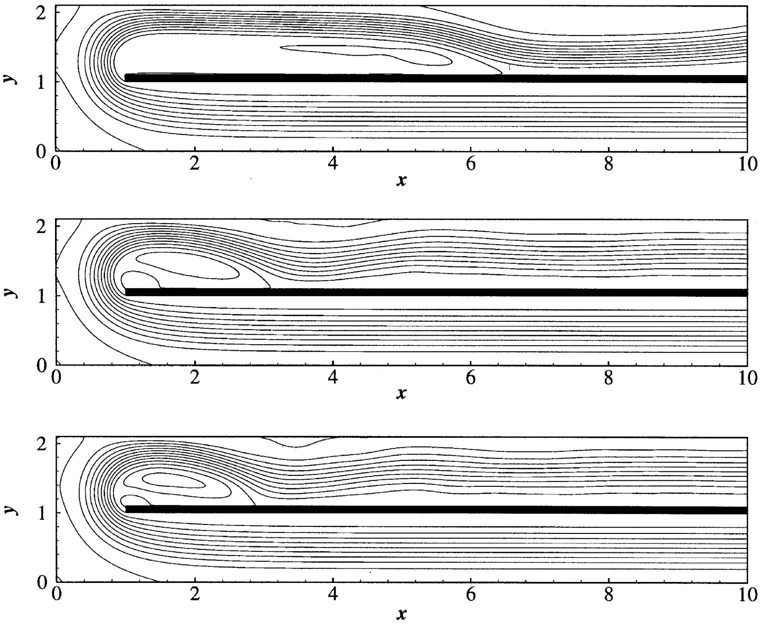

Fig. 9. Contours of time-mean streamlines: (a) $Re = 500$, (b) $Re = 700$ and (c) $Re = 1000$. Increments are $\Delta\psi = 0.1$.

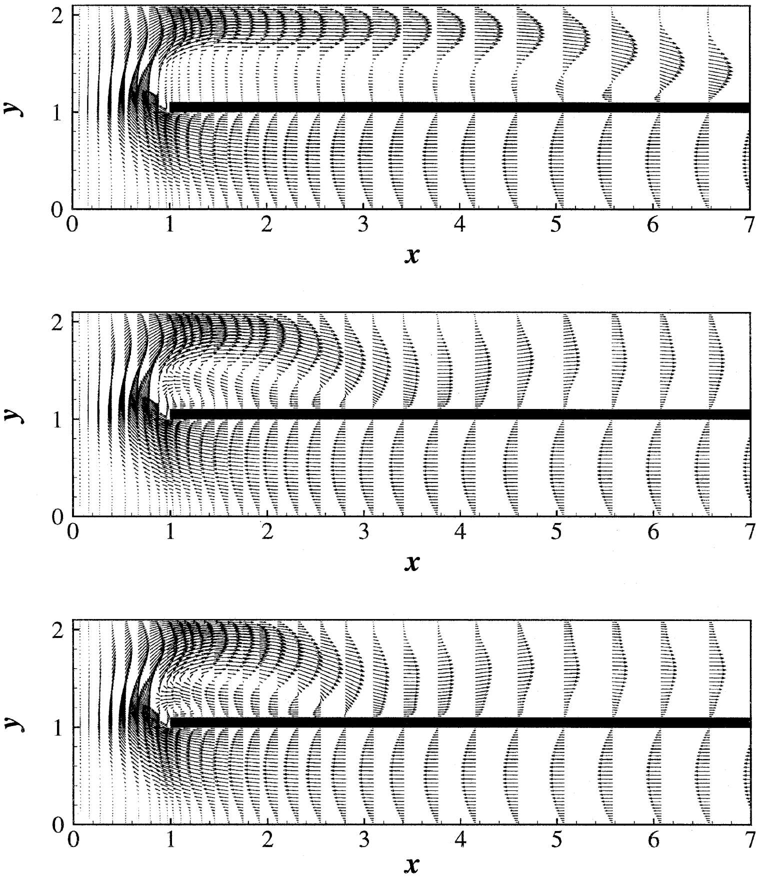

Fig. 10. Vector plots of time-mean flow field: (a) $Re = 500$, (b) $Re = 700$ and (c) $Re = 1000$.

the unsteadiness occurs, the size of the re-circulation region reduces dramatically. The re-attachment length is determined as a distance from the edge of the bend ($x = 1.0$) to a point where the time-mean velocity is zero. At $Re = 500$, the re-attachment length is $x_r = 5.48$ and at $Re = 700$, it reduces to $x_r = 2.10$ (see Fig. 14). At

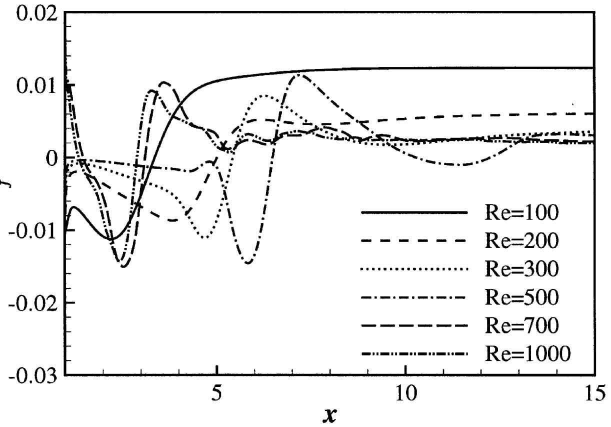

Fig. 11. C_f distributions along the wall (at $y = 1.1$).

Table 1
The re-attachment length x_r and averaged *Nu* along the wall

Re	x_r	Nu_{15}	Nu_5
50	1.13	0.255	0.522
100	2.35	0.325	0.583
150	3.34	0.370	0.577
200	4.00	0.410	0.559
300	4.61	0.551	0.553
400	5.03	0.631	0.467
500	5.48	0.918	0.402
600	4.43	1.110	0.380
700	2.10	1.842	3.363
800	1.75	2.108	4.012
1000	1.89	2.476	4.568

Here, Nu_{15} represents *Nu* averaged for $1 \leqslant x \leqslant 15$ and Nu_5 averaged for $1 \leqslant x \leqslant 5$.

Table 2
The minimum value of C_f and maximum value of *Nu*, and their locations

Re	$C_{f\,\min}$	x_{C_f}	$Nu_{\max}$	x_{Nu}
50	−0.01975	1.052	0.568	2.414
100	−0.01125	2.216	0.701	3.413
150	−0.00922	3.009	0.804	4.27
200	−0.00868	3.799	0.988	4.951
300	−0.01217	4.900	1.793	5.575
400	−0.01423	5.350	2.361	6.025
500	−0.01459	5.850	2.823	6.450
600	−0.01470	6.550	7.175	3.171
700	−0.01508	2.538	5.121	3.065
800	−0.01812	2.198	5.917	2.755
1000	−0.01511	2.442	6.718	2.836

$Re = 500$, the high velocity fluid near the upper wall is separated from the stagnant flow inside the re-circulation region. Consequently, there is minimal mixing between the two regions. In contrast, at $Re = 700$, the mixing inside the re-circulation zone is rather strong. Once the flow becomes oscillatory, the overall flow features do not change much with increasing *Re*.

Fig. 11 shows the C_f distributions at the outlet channel lower wall ($y = 1.1$). Results are also summarised in Tables 1 and 2. It can be seen that the re-attachment length increases with the Reynolds number until $Re \approx 600$. The location of the negative peak (x_{C_f}) also moves downstream with the increasing Reynolds number. This peak value decreases, indicating stronger re-circulating motions. Then, an abrupt change occurs for $Re > 600$. Also, the size of the re-circulation zone is reduced dramatically. As the flow becomes oscillatory, C_f distributions become almost Reynolds number independent.

The dramatic changes caused by the flow oscillation are clearly seen in Fig. 12. This shows instantaneous velocity vectors for $Re = 700$. The flow inside the re-circulation zone is active and the maximum reverse velocity is of the same order of magnitude as the main flow. This is consistent with the high C_f value at $Re = 700$ (Fig. 11).

Fig. 13 shows instantaneous streamlines at time intervals of $\Delta t = 1.0$. Large-scale vortices emanating from the sharp corner are clearly seen. These move downstream at an almost constant velocity. The convection velocity of the large-scale vortices is about 60% of U_m. As seen from Fig. 8, the flow is quasi-periodic forming a complex unsteady flow cycle. It is clear that the large-scale vortex shedding dominates the whole flow field. The amplitude of the flow oscillations decays slowly until as it approaches the computational domain exit.

4.4. Convective heat transfer

In this section, heat transfer is analysed. The main focus is the outlet channel lower wall. The Nusselt number is defined as

$$Nu = \frac{h}{\Delta T}\frac{\mathrm{d}T}{\mathrm{d}y}, \tag{5}$$

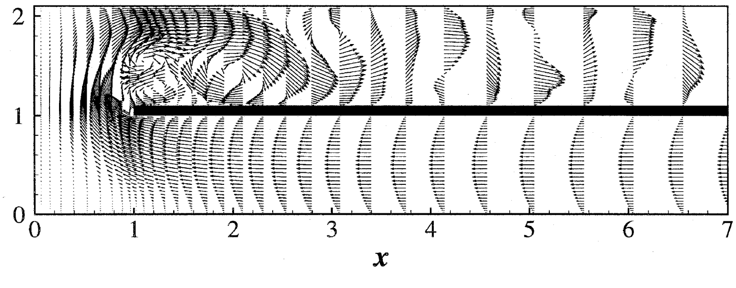

Fig. 12. Vector plots of instantaneous flow field at $Re = 700$.

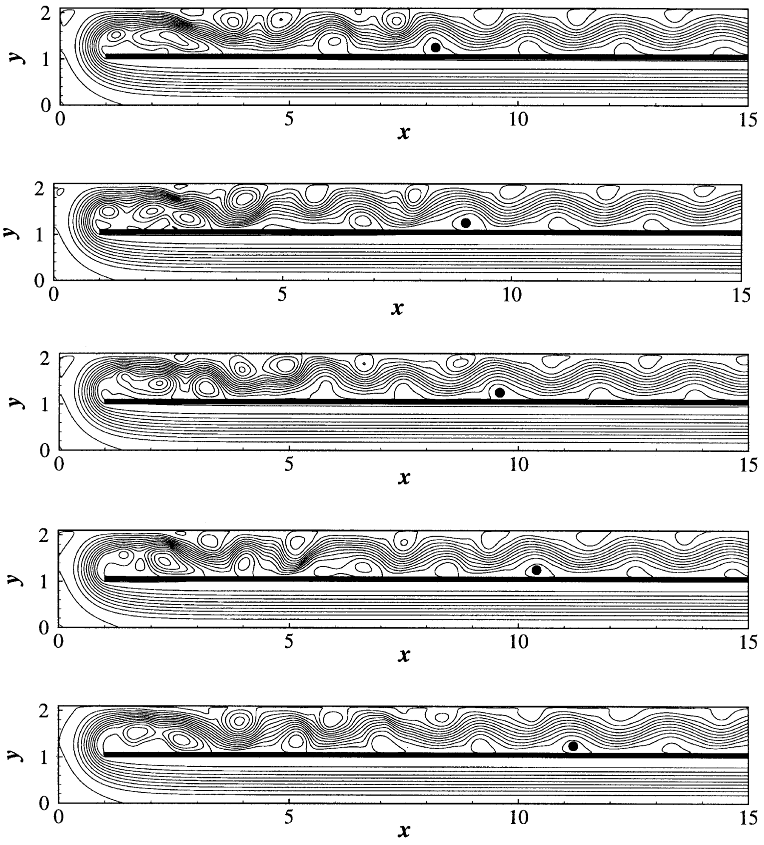

Fig. 13. Contours of instantaneous streamlines at $Re = 700$ for time intervals of $\Delta t = 1.0$.

where ΔT is the temperature difference $(T_w - T_i)$, T_w the wall temperature and T_i the inlet temperature.

Fig. 14 shows the time-mean Nusselt number distribution along the lower wall, located at $y = h + d$. As the flow moves downstream, Nu increases and attains a maximum. It then, due to the development of a boundary layer decreases steadily. The maximum Nusselt number, $Nu_{\max}$, rises with Re (see also Table 2). Also, for $Re \leqslant 600$, the $Nu_{\max}$ location moves downstream with increasing Re. Analysis shows the maximum Nusselt number occurs just downstream of the time-mean re-attachment points. At $Re = 500$, $Nu_{\max}$ is an order of magnitude larger than Nu in the re-circulation zone. As the flow becomes oscillatory ($Re = 700$), the Nu distribution shows a very different pattern from the gradual steady regime ($Re \leqslant 600$) changes. Nu is increased substantially in the whole region. The $Nu_{\max}$ location suddenly moves upstream. Also, the region where Nu is small ($Nu < 1$) has almost disappeared. At further higher Reynolds numbers, the Nu distribution shows similar trends to that for $Re = 700$. These findings are consistent with the C_f distributions as shown in Fig. 11.

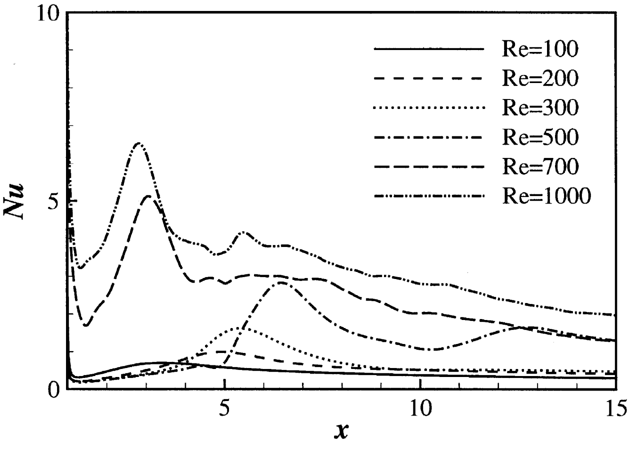

Fig. 14. Nu distributions along the lower wall (at $y = 1.1$).

To investigate the correlation between the flow and temperature field, x_r and Nu are presented together in Fig. 15. Here, Nu_{15} represents Nu averaged along the wall ($1 \leqslant x \leqslant 15$). The reduction in x_r and increase in Nu with the onset of oscillatory flow ($Re > 600$) are clear. To emphasise the effect of flow unsteadiness in the re-circulation region, another Nu_5 average over a short distance ($1 \leqslant x \leqslant 5$) is provided. This region corresponds to the recirculation zone at $Re = 300$. The increase in Nu_5 due to unsteadiness is dramatic.

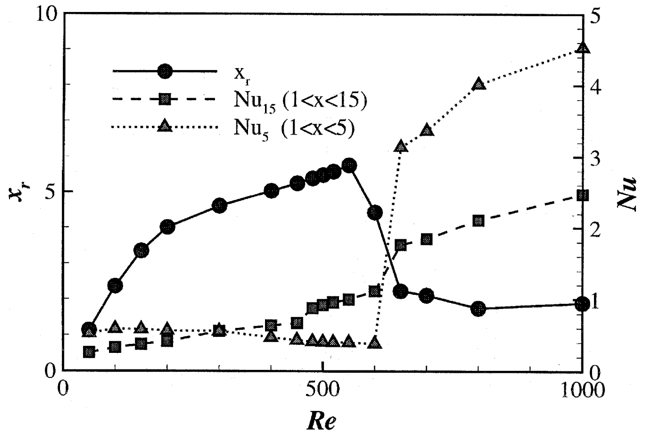

Fig. 15. x_r and average *Nu* as a function of *Re*. Nu_{15} is *Nu* averaged along the wall for $1 \leqslant x \leqslant 15$ and Nu_5 for $1 \leqslant x \leqslant 5$.

4.5. Instantaneous heat transfer

To investigate the effect of flow oscillation on the unsteady convective heat transfer, instantaneous flow and temperature fields for $Re = 700$ are analysed. Fig. 16(a) and (b) shows contour plots of streamfunction and temperature at the same time instant. As the large-scale vortices move downstream, the temperature field also shows oscillatory behaviour. As expected, heat transfer is decreased in the re-circulation regions. Downwards motions between vortices enhance the heat transfer significantly. This is reminiscent of impinging jet heat transfer (see Chung et al., 2002).

Instantaneous C_f and *Nu* distributions along the wall are also shown in Fig. 16(c). The oscillatory part of C_f and *Nu* is significant compared to the mean values. Also, the instantaneous *Nu* distribution correlates well with wall shear stress. As expected, the location for minimum C_f is consistent with the location of the large-scale vortices. The minimum *Nu* is located a little *upstream* of the minimum C_f. This is because of thermal boundary layer thickening. Similar characteristics have been observed in unsteady impinging jets (Chung et al., 2002). Analysis shows the active heat transfer region, corresponding to the maximum local Nusselt number, is convecting downstream at a constant speed. In the main separation region, the correlation between heat transfer and flow field is not so good as further downstream. This is because, around the main separation region there are many smaller secondary vortices (see Figs. 12 and 13). Further downstream of the main separation region the small-scale vortices merge to produce a more coherent flow field (see Fig. 13). Then the correlation between heat transfer and flow field improves.

5. Concluding remarks

Numerical simulations of unsteady laminar flow around a sharp 180° bend are performed for $50 \leqslant Re \leqslant 1000$. Extensive studies are conducted to verify the numerical methods used. Verification results show good agreement with available data for three test cases. The

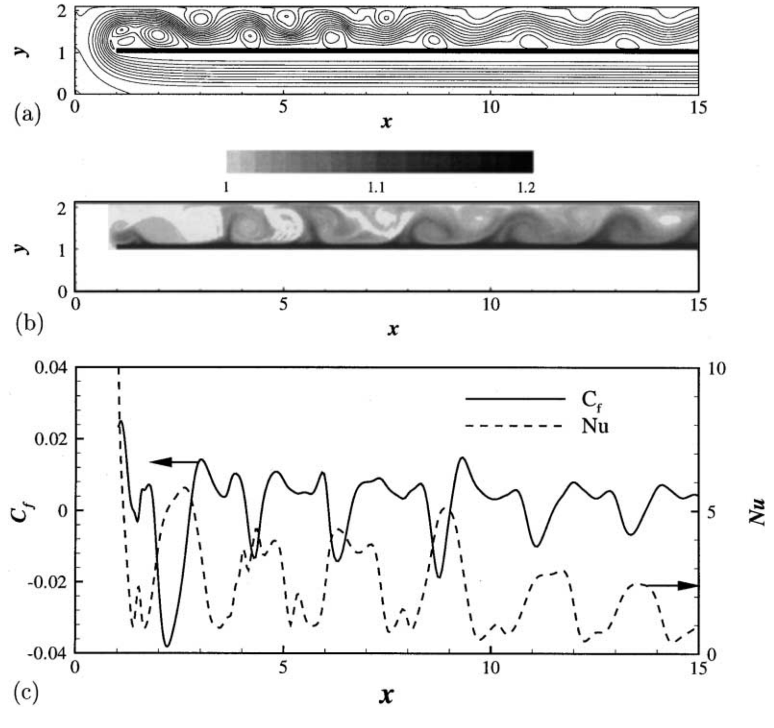

Fig. 16. Instantaneous streamfunction (top) and temperature (middle) plots, and C_f and *Nu* distributions along the wall (bottom) at $Re = 700$.

side wall effects are found to be small even at moderate aspect ratio ($\mathrm{AR} = 5$) as the secondary vortices are confined to the side wall region. The flow in the central part can be regarded as two-dimensional. Predictions also show the sharp bend flow remains steady until $Re \approx 600$. However, a further increase in the Reynolds number gives rise to oscillatory flow. Oscillations cause a substantial reduction in the re-attachment length and a dramatic increase in convective heat transfer. For $Re = 700$, the re-attachment length is reduced to less than half and the Nusselt number increases several times compared to $Re = 600$ case. The correlation between flow structure and heat transfer is found to be strong. It is found that the onset of flow oscillations is important as it dramatically enhances heat transfer.

Acknowledgements

The support of the Engineering and Physical Sciences Research Council (EPSRC) of the United Kingdom under grant number GR/N05581 is gratefully acknowledged. We thank Dr. Andrey V. Boiko for valuable discussions on three-dimensional flow instability.

References

Armaly, B.F., Durst, F., Peieira, J.C.F., 1983. Experimental and theoretical investigation of backward-facing step flow. J. Fluid Mech. 127, 473–496.

Beitelmal, A.H., Saad, M.A., Patel, C.D., 2000. The effect of inclination on the heat transfer between a flat surface and an impinging two-dimensional air jet. Int. J. Heat Fluid Flow 21, 156–163.

Brederode, P., Bradshaw, P., 1978. Influence of the side walls on the turbulent center-plane boundary-layer in a squareduct. ASME: J. Fluids Engng. 100, 91–96.

Chung, Y.M., Sung, H.J., Boiko, A.V., 1997. Spatial simulation of the instability of channel flow with local suction/blowing. Phys. Fluids 9 (11), 3258–3266.

Chung, Y.M., Luo, K.H., Sandham, N.D., Williams, J.J.R., 2001a. Direct numerical simulation of an impinging jet. In: Lindborg, E., Johansson, A., Eaton, J., Humphrey, J., Kasagi, N., Leschziner, M., Sommerfeld, M. (Eds.), Turbulence and Shear Flow Phenomena, vol. 2. Universitetsservice US AB, Stockholm, pp. 271–276.

Chung, Y.M., Tucker, P.G., Luo, K.H., 2001b. Large-eddy simulation of complex internal flows. In: Geurts, B.J., Friedrich, R., Mètais, O. (Eds.), Direct and Large-Eddy Simulation, vol. IV. Kluwer Academic Publishers, The Netherlands, pp. 373–380.

Chung, Y.M., Luo, K.H., Sandham, N.D., 2002. Numerical study of momentum and heat transfer in unsteady impinging jets. Int. J. Heat Fluid Flow 23, 592–600.

Chyu, M.K., 1991. Regional heat transfer in two-pass and three pass passages with 180° sharp turn. ASME: J. Heat Transfer 113, 63–70.

Ghaddar, N.K., Karczak, K.Z., Mikic, B.B., Patera, A.T., 1986. Numerical investigation of incompressible flow in grooved channels. Part 1: Stability and self-sustained oscillations. J. Fluid Mech. 163, 99–127.

Ghia, K.N., Sokhey, J.S., 1977. Laminar incompressible viscous flow in curved ducts of regular cross-sections. ASME: J. Fluids Engng. 99, 640–648.

Hille, P., Vehrenkamp, R., Schulz-Dubois, E.O., 1985. The development and structure of primary and secondary flow in a curved square duct. J. Fluid Mech. 151, 219–241.

Hirota, M., Fujita, H., Syuhada, A., Araki, S., Yoshida, T., Tanaka, T., 1999. Heat/mass transfer characteristics in two-pass smooth channels with sharp 180° turn. Int. J. Heat Mass Transfer 42, 3757–3770.

Kim, J., Moin, P., 1985. Application of a fractional-step method to incompressible Navier–Stokes equations. J. Comput. Phys. 59, 308–323.

Kim, S.Y., Kang, B.H., Hyun, J.M., 1997. Forced convection heat transfer from two heated blocks in pulsating channel flow. Int. J. Heat Mass Transfer 41, 625–634.

Kleiser, L., Zang, T.A., 1991. Numerical simulation of transition in wall-bounded shear flows. Ann. Rev. Fluid Mech. 23, 495–537.

Liou, T.-M., Chen, C.-C., Tzeng, Y.-Y., Tsai, T.-W., 2000. Non-intrusive measurements of near-wall fluid flow and surface heat transfer in a serpentine passage. Int. J. Heat Mass Transfer 43, 3233–3244.

Metzger, D.E., Sahm, M.K., 1986. Heat transfer around sharp 180° turns in smooth rectangular channels. ASME: J. Heat Transfer 108, 500–506.

Mochizuki, S., Murata, A., Shibata, R., Yang, W.-J., 1999. Detailed measurements of local heat transfer coefficients in turbulent flow through smooth and rib-roughened serpentine passages with a 180° sharp bend. Int. J. Heat Mass Transfer 42, 1925–1934.

Pauley, L.R., Moin, P., Reynolds, W.C., 1990. The structure of two-dimensional separation. J. Fluid Mech. 220, 397–411.

Roychowdhury, D.G., Das, S.K., Sundararajan, T., 1999. An efficient solution method for incompressible N–S equation using non-orthogonal collocated grid. Int. J. Numer. Meth. Engng. 45, 741–763.

Tucker, P.G., Pan, Z., 2001. URANS computations for a complex internal isothermal flow. Comput. Meth. Appl. Mech. Engng. 190, 2843–2907.

Van Doormaal, J.P., Raithby, G.D., 1984. Enhancements of the SIMPLE method for predicting incompressible fluid flows. Numer. Heat Transfer 7, 147–163.